Bathymetry in Petermann fjord from Operation IceBridge aerogravity

Kirsty J. Tinto [a,*], Robin E. Bell [a], James R. Cochran [a], Andreas Münchow [b]

[a] *Lamont-Doherty Earth Observatory of Columbia University, Palisades, NY, USA*
[b] *College of Earth, Ocean and Environment, University of Delaware, Newark, DE, USA*

A B S T R A C T

Petermann Glacier is a major glacier in northern Greenland, maintaining one of the few remaining floating ice tongues in Greenland. Monitoring programs, such as NASA's Operation IceBridge have surveyed Petermann Glacier over several decades and have found it to be stable in terms of mass balance, velocity and grounding-line position. The future vulnerability of this large glacier to changing ocean temperatures and climate depends on the ocean–ice interactions beneath its floating tongue. These cannot currently be predicted due to a lack of knowledge of the bathymetry underneath the ice tongue. Here we use aerogravity data from Operation IceBridge, together with airborne radar and laser data and shipborne bathymetry-soundings to model the bathymetry beneath the Petermann ice tongue. We find a basement-cored inner sill at 540–610 m depth that results in a water cavity with minimum thickness of 400 m about 25 km from the grounding line. The sill is coincident with the location of the melt rate minimum. Seaward of the sill the fjord is strongly asymmetric. The deepest point occurs on the eastern side of the fjord at 1150 m, 600 m deeper than on the western side. This asymmetry is due to a sedimentary deposit on the western side of the fjord. A 350–410 m-deep outer sill, also mapped by marine surveys, marks the seaward end of the fjord. This outer sill is aligned with the proposed Last Glacial Maximum (LGM) grounding-line position for Petermann Glacier. The inner sill likely provided a stable pinning point for the grounding line in the past, punctuating the retreat of Petermann Glacier since the LGM.

© 2015 Published by Elsevier B.V.

## 1. Introduction

1.1. Petermann Glacier

Petermann Glacier in northern Greenland (80.5°N, 60°W) drains 4% of the Greenland Ice Sheet and discharges $\sim$12 ± 1 Gt/yr (Rignot and Steffen, 2008) of ice into a 90 km-long, 20 km-wide fjord (Fig. 1). Ice is 600 m thick at the grounding line, and supports a long floating ice tongue. In 2011, this tongue was 53 km-long and 150 m-thick at its calving front. Petermann Glacier is generally stable, with little observed change in surface elevation (Pritchard et al., 2009), grounding-line position (Rignot, 1998) or velocity (Moon et al., 2012), and velocities ranging from 100 m/yr in the interior to $\sim$1000 m/yr at the grounding line. Ice islands, large tabular icebergs, calve periodically from the front of the tongue, but over a decadal timescale the calving front is also considered stable (Münchow et al., 2014).

Mass loss from the Greenland ice sheet is influenced both by a warming atmosphere and the warming ocean. Neighboring glaciers often show variable responses to changing regional controls (Moon et al., 2012; Porter et al., 2014), suggesting that processes within the fjords that connect glacier grounding lines to ocean waters could play an important role in governing glacier behavior. Petermann Glacier is of particular interest as it supports one of the few remaining ice tongues in northern Greenland. Khan et al. (2010) observed a pattern of enhanced mass loss that has moved clockwise around Greenland towards the north–west, and which could potentially change the mass balance of northern Greenland from stable to unstable. It is still unclear how the 2010 and 2012 large calving events may have changed the force balance of this glacier that potentially lead to acceleration, dynamic thinning, and thus enhanced mass loss. Model results by Nick et al. (2012) conclude that neither 2010 nor 2012 calving events disturb the force balance, however, the same model also indicates large sensitivity to basal melting by the ocean. Such melt rates reflect ocean dynamics that are impacted by details of the bottom topography.

The bathymetry under the floating tongue is one of the outstanding unknowns in understanding the interactions between
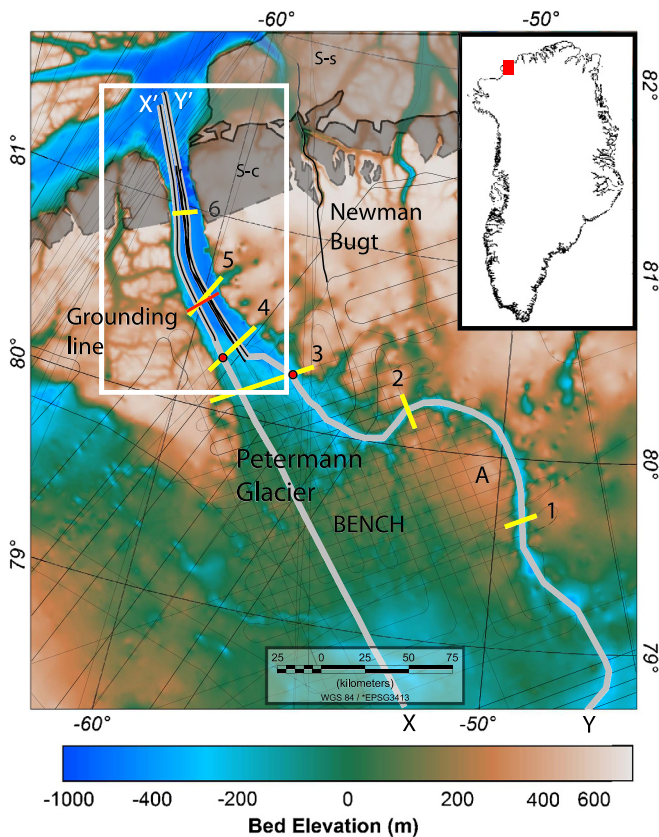
Fig. 1. The onshore catchment of Petermann Glacier. Grounding line is shown in red. Grey lines (X–X′ and Y–Y′) are longitudinal profiles of the deep canyon shown in Fig. 6a, red circles show position of rebounded shoreline. Yellow lines show position of cross sections in Fig. 6c. A marks the interpreted igneous body at the eastern end of the raised bedrock bench. The curving grey line marks the route of the deep canyon. Topography from Bamber et al. (2013a). Red box shows area of Fig. 3. (For interpretation of the references to color in this figure legend, the reader is referred to the web version of this article.)

the ocean and ice in Petermann fjord (Johnson et al., 2011). Radar surveys provide measurements of bed topography where ice is grounded, and ship surveys measure bathymetry at the seaward end of the fjord (Johnson et al., 2011), but the bathymetry under the floating tongue remains unknown. Constraining the bathymetry of this area provides important boundary conditions for models of water circulation within Petermann fjord, and reveals some of the history of glacial erosion and deposition within the fjord. Here, we invert gravity anomalies measured as part of NASA's Operation IceBridge (OIB) to model the bathymetry beneath the floating tongue of Petermann Glacier and investigate the influence of this bathymetry on the behavior of the glacier.

1.2. Petermann catchment morphology

The Petermann catchment extends over 300 km from its grounding line into the interior where the ice is 2300 m thick, and the bed is 250 m below sea level (Fig. 1). Bed topography, gravity and magnetic anomalies have been mapped by Operation IceBridge, as described below, to establish the morphology and geology of the catchment (Fig. 2). An 85 km-wide elevated bench in the bed topography with bed elevation 0–100 m above sea level and ice thickness of 1600 m, crosses the width of the catchment 150 km inland from the grounding line, near 79.5°N latitude (Fig. 1). Bed elevation lowers to below sea level to the north of the bench where the eastern side of the catchment is ~200 m deeper than the west. In this region, the flow is confined within a 65 km-wide channel that narrows to become the

20 km-wide fjord (Fig. 1). At the grounding line, ice thickness is ~600 m and the bed elevation 410–480 m below sea level (Allen, 2011). The grounding line depth is asymmetric with the eastern side 70 m deeper than the west, similar to the asymmetry observed in the area between the grounding line and the bench, where the eastern side is deeper than the west. The deep eastern side of the Petermann catchment north of the topographic bench is the continuation of a 750 km-long, 500 m-deep canyon that can be traced from the interior of Greenland (Van der Veen et al., 2007; Bamber et al., 2013b) (Fig. 1). The canyon route is diverted to the east around the 100 m a.s.l. bench in the Petermann catchment. At the eastern end of this bench, a 50 km-wide, circular topographic high rises 300 m above the main bench. This eastern high has a smooth surface with little evidence of dissection, in contrast with the main bench, which is cut by channels up to 200 m deep and tens of meters wide. Gravity and magnetic data over the circular high reveal a high Bouguer anomaly and high magnetic anomaly, supportive of the topographic high being an intruded igneous body (Fig. 2b and c). The canyon closely traces the edge of this body, turning through 180 degrees and continuing down towards the Petermann fjord.

The Petermann fjord cuts through metasediments of the Cambrian–Devonian Franklin Basin that were metamorphosed in the Devonian–Carboniferous Ellesmere fold belt and currently dip gently to the north with an approximately east–west strike (Henriksen et al., 2009). These metasediments are exposed in the ~900 m-high walls of Petermann fjord. At the northern end of the fjord where the walls are lower, east–west striking Silurian carbonate reefs are exposed on land as a distinctive ridge coincident with the outermost part of the fjord (Henriksen et al., 2009). The higher parts of this sedimentary sequence, including the Silurian reefs, are also exposed in the walls of Newman Bugt, the next fjord to the east.

2. Methods

2.1. Surveys

Operation IceBridge is a multi-year campaign of airborne geophysical surveys, providing a complete cross-section of the ice sheet under the survey lines. Ice surface elevation is monitored by the NASA Airborne Topographic Mapper (ATM) lidar to an accuracy of ~10 cm (Krabill et al., 2002). Ice thickness and internal structure are recorded by the Multi-channel Coherent Radar Depth Sounder (MCoRDS) radar developed by the University of Kansas' Center for Research on Ice Sheets (CReSIS) with ~10 m accuracy (Leuschen, 2012). The magnetic field is measured with a Scintrex CS-3 Cesium magnetometer (accurate to 7 nT along a repeated track) (Cochran et al., 2011). The gravity field is measured using a Sander Geophysics Ltd AIRGrav system (Argyle et al., 2000; Sander et al., 2004; Cochran and Bell, 2011). There are no flightline crossovers in the lines along Petermann Fjord, but an analysis of a grid survey in the Petermann catchment (Fig. 2) shows a standard deviation of 0.9 mGal for 225 crossing points. An analysis of repeat IceBridge gravity lines in Greenland, which is a better way to assess the repeatability of measurements due to the along-track directionality of filtering, gives an RMS difference of 0.72 mGal for data processed with a 70 s temporal filter (Boghosian et al., submitted for publication), which is the filter applied to the data used in this study.

An advantage of the AIRGrav system is that it is able to collect high-quality data on flight with flight elevation changes (Studinger et al., 2008). OIB flights are typically flown draped at a nominal 500 m above ground level, sometimes lowering to 200 m over open water. Where the bed elevation is unknown under floating ice or where no bed return is detected in radar, the gravity anomaly can be inverted to model the elevation and shape of the
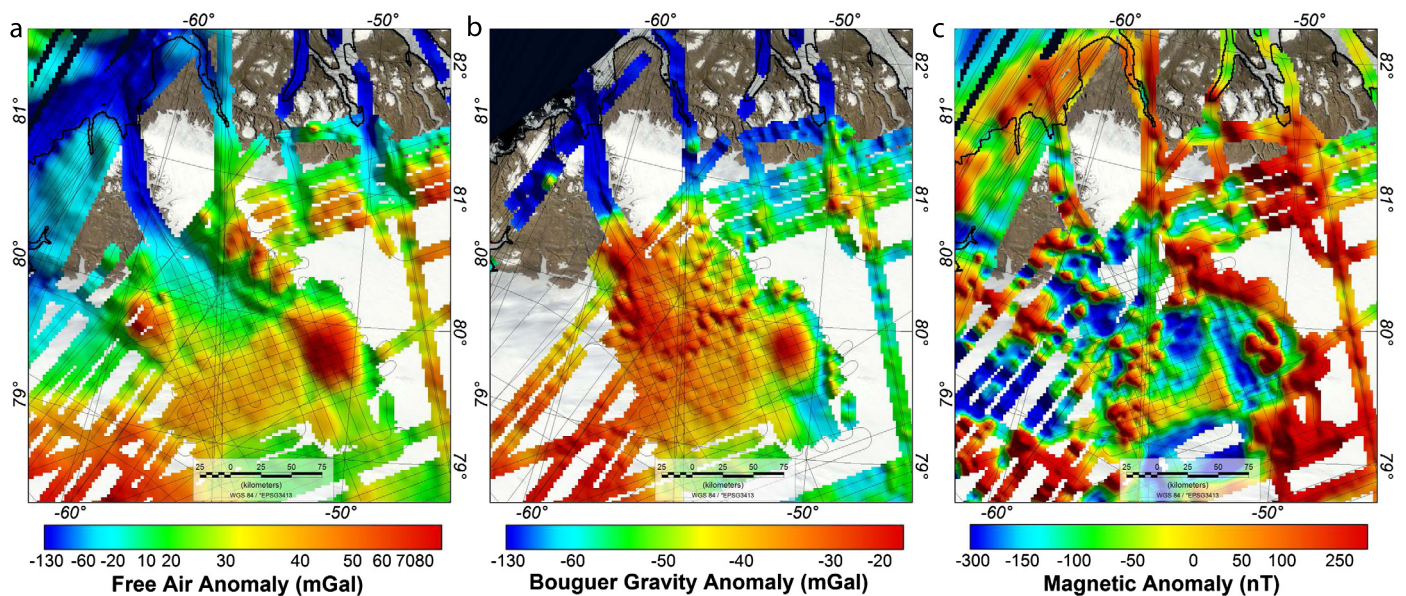
Fig. 2. a) Free-air gravity anomalies from OIB flights during 2009–2011. b) Bouguer gravity anomalies from OIB flights during 2009–2011. c) Magnetic anomalies from OIB flights during 2009–2011. Flight lines are shown in grey.

bed. Magnetic anomalies vary with distance from a magnetic body, and with the susceptibility and remanence of the body, and so are used to constrain geological variations that can contribute to the gravity anomaly and to estimate the depth to crystalline basement.

OIB has flown six survey lines along the axis of Petermann Glacier and fjord (Fig. 3a). Two lines flown on 7 May 2011 surveyed the eastern (A–A′) and western (B–B′) sides of the Petermann fjord and continued across open water (Fig. 3). Three shorter lines, flown on 24th March and 20th April 2010, without a magnetometer, are clustered on the eastern side of the fjord and record smaller scale spatial variability. The maximum separation of these lines is approximately 2.5 km, with one repeating the track of line A–A′ to within 100 m lateral separation. A sixth, high elevation line flown along the axis is not analyzed in depth in this study, as the short-wavelength signal from bathymetry has been attenuated by the high survey elevation. Additional constraints are available from marine-based surveys from the Canadian Coastguard icebreaker *Henry Larsen* that measured bathymetry at the head of the fjord in 2009 (Johnson et al., 2011) and inside the fjord up to the 2012 calving front located 45 km seaward of the grounding line (Fig. 3b).

2.2. Gravity inversion

The bathymetry of the sea floor under the floating ice tongue is unknown, and so we model the bathymetry by inverting the observed gravity anomaly. The inversion was performed using the Geosoft GMSys software package, which is based on the technique of Talwani et al. (1959). We create a gravity model by assuming three bodies (ice, rock and water) with different densities. Ice has a density of 915 kg/m^3 and its boundaries are defined by the ATM lidar surface and the MCoRDs-derived ice thickness. Rock is assigned a density of 2670 kg/m^3 and its upper surface is defined by radar sounding over grounded ice and marine bathymetry surveys over water. Sea water is assigned a density of 1028 kg/m^3.

Over the areas where bed topography is known the predicted gravity anomaly has the same shape as the observed gravity anomaly, but the simple, three-body model fails to reproduce the long-wavelength components of the observed anomaly. The residual between predicted and observed anomalies increases along the profile as a result of this long-wavelength signal reaching a maximum mismatch of 55 mGal. Variations in crustal thickness or

density variations within the mantle can produce long-wavelength anomalies that are not accounted for in the three-body model. As we have no independent constraints on the crustal and mantle structure of northern Greenland, we removed the long-wavelength component of the observed gravity anomaly by subtracting a regional field. The regional field was derived from the WGM2012 free-air gravity anomaly (Balmino et al., 2011), upward-continued to 40 km so that the gravity signature of topographic features was no longer resolvable.

We tested this regional correction on a profile along the neighboring fjord, Newman Bugt (Fig. 4). Here the topography of both the northern and southern ends of the profile are known from Ice-Bridge radar and lidar, and Paleozoic metasediments are exposed at the northern end of the profile with negligible recent sediment cover. We used the known bed topography to model the predicted gravity of Newman Bugt, using a reference density column at the southern end of the profile. Without accounting for the regional field, the predicted and observed anomalies showed a 25 mGal difference at the northern end of the 130 km long profile. By removing the regional field from the observed gravity this residual was reduced to zero. We therefore used the 40 km upward continued WGM2012 regional field to account for the long-wavelength components of the gravity anomaly along Petermann fjord.

After accounting for the regional field in Petermann fjord, and using a reference density column at the southern end of the profiles, residuals between the calculated (Fig. 5, dashed green line) and observed (Fig. 5, solid teal line) gravity persist over the northern, seaward end of profiles, where bathymetry is constrained by ship-based observations. On the eastern profile, the maximum residual is 22 mGal and on the western profile, it is 39 mGal. These residuals suggest that shorter-wavelength density variations, caused by changes in geology at shallow depths exist within the fjord in addition to the deeper variations accounted for by the regional correction. Possible geological interpretations are discussed below, but in order to construct a bathymetry model, we approximated the effect of shallow geological variations by applying a linear correction to the predicted gravity to provide a best fit between the constraints of the grounded ice and those of the marine bathymetry. We then inverted the observed gravity to create a bathymetry model of the region under the floating ice.
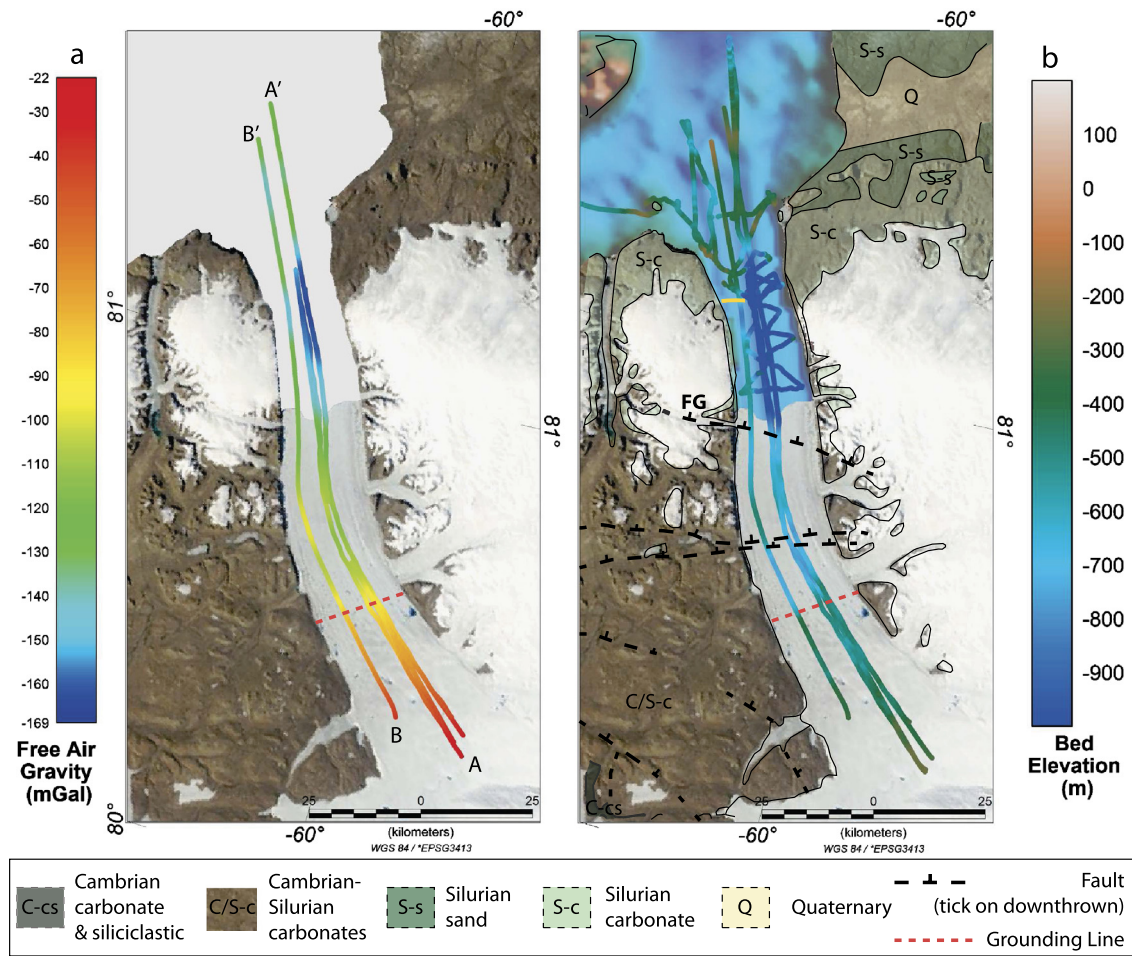
Fig. 3. a) Free-air gravity of Petermann fjord along five Operation IceBridge Survey lines from 2010 and 2011. Approximate grounding line position marked as dotted red line. Modeled profiles A–A′ and B–B′ are shown in Fig. 5. b) Bathymetry of Petermann fjord from inverted gravity anomaly and ship-based surveys. Location of geological boundaries and faults from Escher and Pulvertaft (1995) and Jensen (1998) after Bengaard and Henriksen (1991) and Jepsen et al. (1983). **FG** is the Faith Gletscher fault. Location of newly proposed fault is shown in yellow. (For interpretation of the references to color in this figure legend, the reader is referred to the web version of this article.)
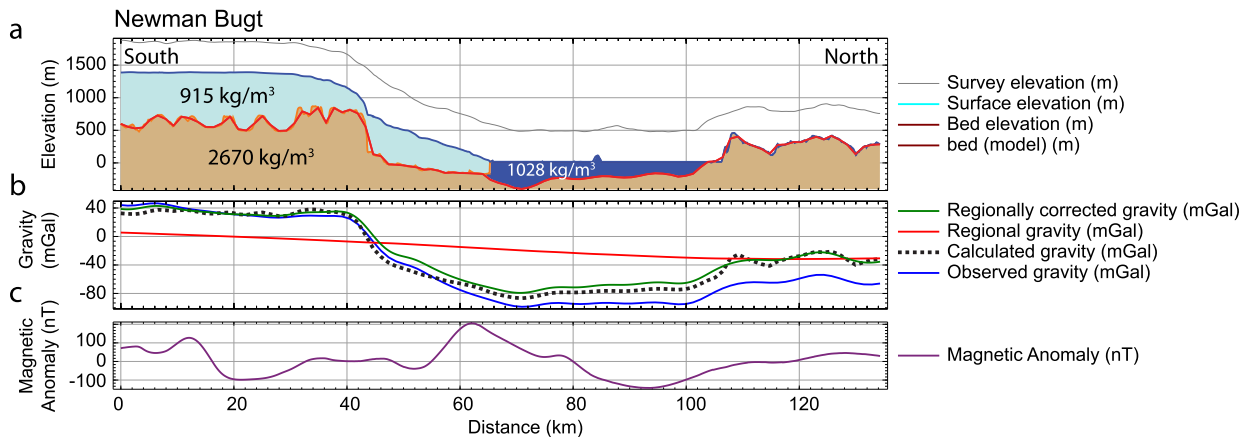

Fig. 4. Profile of Newman Bugt (location shown in Fig. 1) showing effectiveness of regional correction. a) Geometry of ice, rock, and survey elevation. b) Gravity anomaly, calculated (black), regional (red), observed (blue) and observed-minus-regional (green). c) Observed magnetic anomaly. Geometry of rock–water interface is modeled from inversion of observed-minus-regional field. (For interpretation of the references to color in this figure legend, the reader is referred to the web version of this article.)

Of the various sources that could influence the gravity anomaly, the density contrast between rock and water at the seafloor is the strongest and the nearest to the measurement platform, and so is expected to make the greatest contribution to the model. For this reason we expect the shape of the modeled bathymetry to be correct, even when there is uncertainty in the absolute depth

determination. We assessed the uncertainty of the model by considering both the modeling process and instrument accuracy. Uncertainty due to unconstrained geological variations is established by comparing the models where no linear correction is applied and where the reference density column is taken from either the southern, radar-constrained or northern, acoustically-constrained
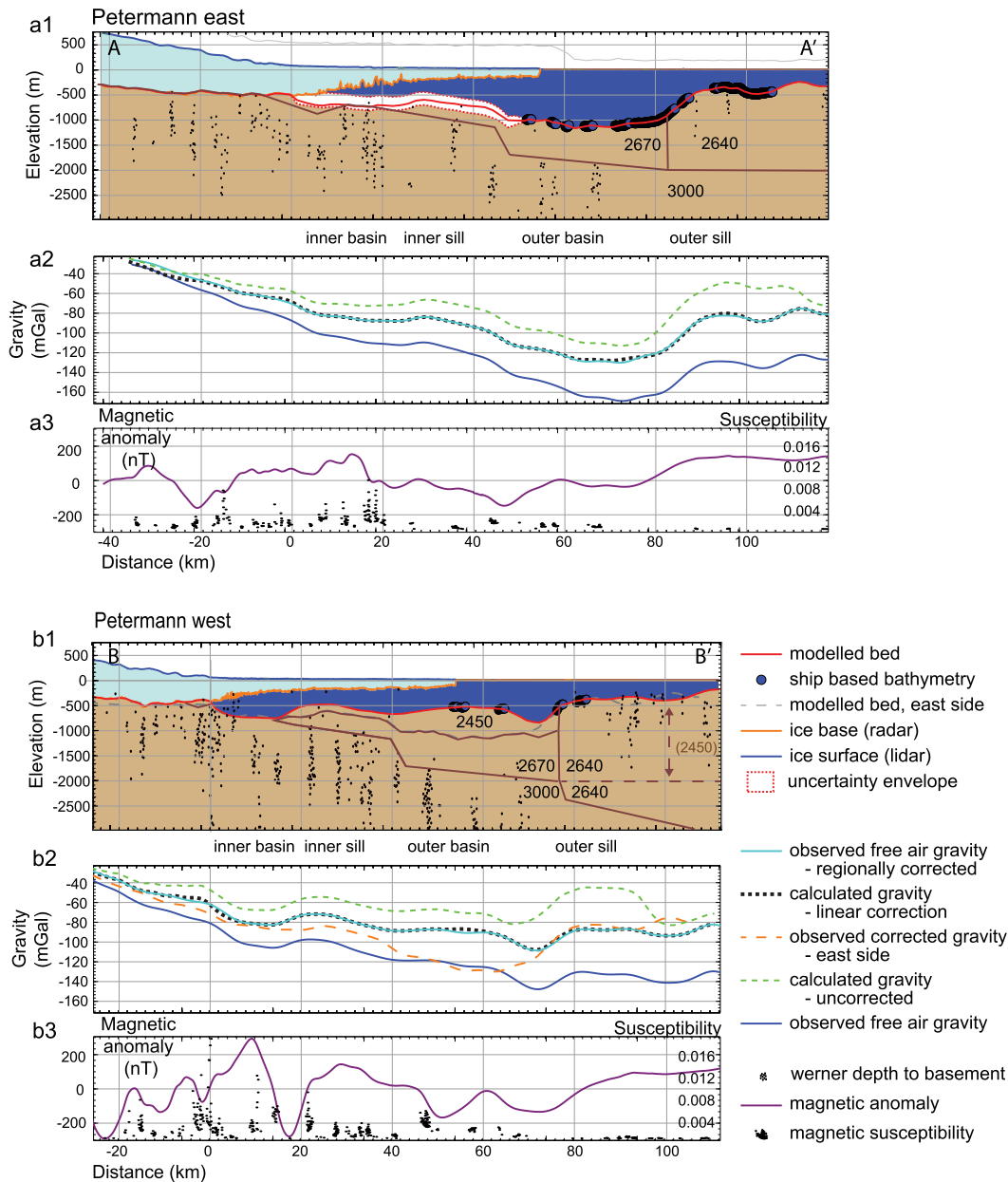
Fig. 5. Profiles of Petermann East (a1, a2, a3) and West side (b1, b2, b3) (location shown in Fig. 1). 1) Geometry of ice, rock, and survey elevation. Magnetic depth to basement solutions from Werner deconvolution are marked as dots. White envelope on a1 represents uncertainty of bathymetry inversion on eastern (B–B′) profile. Brown lines show geological boundaries, with density of blocks in kg/m³ marked in black text. 2) Gravity anomaly, calculated (green dashed), calculated with linear correction (black), observed (blue) and observed-minus-regional (green). Orange dashed line on b2 shows gravity from eastern profile superimposed on western profile. 3) Observed magnetic anomaly (line) and modeled magnetic susceptibility from Werner deconvolution (dots). Geometry of rock–water interface is modeled from inversion of observed-minus-regional field. (For interpretation of the references to color in this figure, the reader is referred to the web version of this article.)

ends of the profile. The resulting uncertainty envelope is shown in Fig. 5. The mean width of this envelope is 248 m, giving an uncertainty due to geological variations of approximately ±124 m. The total uncertainty of the bathymetry model also includes instrument accuracy. The accuracy of the gravimeter is included in the RMS fit between modeled and observed gravity in each profile. The forward-modeled gravity anomaly fits the observed with a root mean squared (RMS) error of 1.78 mGal on the east side and 1.27 mGal on the west. We take the 1.78 mGal error and apply a simple Bouguer slab calculation for a density contrast of 1640 kg/m³ between rock and water to establish a gravity measurement and model-derived depth uncertainty of ± 26 m. The total uncertainty therefore comprises ±124 m from geological uncertainties, ±26 m from gravity measurement and model uncer-

tainties and ±10 m from uncertainty in the radar-derived bed elevation, which defines the bed elevation in the reference density column. This gives a total uncertainty of the model of ±160 m.

2.3. Werner deconvolution

When modeling bathymetry from the observed gravity anomalies, we identified residuals between modeled and observed anomalies that indicate short-wavelength variations in geology along the fjord. The bathymetry model does not attempt to model these variations, but instead their effects are distributed evenly across the profile, with a conservative error envelope that encompasses the effects of any reasonable variation in density along the profile. In order to investigate the geological variations within the fjord, we examined the magnetic anomalies, also acquired by Op-

eration IceBridge during the 2012 survey season. The magnetic anomaly depends on both the depth and the susceptibility of the magnetic source, providing additional constraints on the geology of Petermann Fjord. We use Werner deconvolution (Werner, 1953) as implemented in the Oasis Montaj software package to investigate the variation of depth and susceptibility of magnetic bodies along the profile, and then use this to inform the geological interpretation of Petermann fjord. We assume that sediment fill within the fjord has negligible susceptibility, and that the bedrock beneath the fjord constitutes the magnetic basement.

Werner deconvolution considers a range of wavelengths in moving windows along the profile to analyze the wavelengths of anomaly represented at each point (Werner, 1953). Deeper magnetic sources will contribute longer-wavelength signals to the total anomaly. Potential sources are modeled as dykes or contacts, and their corresponding depths are plotted on the profile and tend to form vertical streaks. The depth to magnetic basement is identified as the top of these streaks (Fig. 5). In this analysis we have plotted only clusters of solutions, where 5 or more solutions are identified within a 100×100 m window. Both the depth to source and the susceptibility of the magnetic material controls the magnitude of the magnetic anomaly, so each depth estimate has a corresponding susceptibility estimate.

3. Results

3.1. Bathymetry of Petermann fjord

Our model of the bathymetry beneath the floating ice tongue (Figs. 3b, 5) identifies a previously unknown and significant inner sill 25 km from the grounding line, bounded by an inner basin on its southern side and an asymmetric outer basin to the north between the inner and outer sill. In the inner basin, the bed reaches a maximum depth of 675 m, 12 km from the grounding line. The minimum depth of the inner sill is 540–610 m at about 25 km from the grounding line. North of the inner sill, the bed deepens into an outer basin with a maximum depth of 1150 m before rising again to the outer sill at the head of the fjord, identified in marine surveys as 410–350 m deep and 85 km from the grounding line (Johnson et al., 2011). The western flight line (Fig. 3 A–A′) runs between the tracks of marine surveys and confirms the continuity of the outer sill across the fjord. Ice thickness over the inner sill is 150–200 m, leaving a 400 m-thick water cavity, similar to the water column thickness over the outer sill.

Differences between the eastern and western bathymetry models reveal an asymmetry across the fjord, which is also shown by marine surveys that reached deep into the fjord to within 45 km of the grounding line in 2012. The grounding line and the crest of the newly-identified inner sill are both 70 m deeper on the east side than on the west, while the deepest part of the fjord, in the outer basin, is 300–600 m deeper on the east, reaching a maximum depth of 1150 m. A cross-section of the outer basin shows a distinct step in elevation marking a submarine escarpment on the western side that runs parallel to the fjord axis (Fig. 6c, profile 6).

3.2. Magnetic depth to basement

The magnetic anomaly shows similar characteristics along both sides of Petermann fjord, although the western side has a peak amplitude of ∼300 nT while the eastern peak is ∼150 nT. On both sides of the fjord the magnetic anomaly has shorter wavelengths and higher amplitudes over the grounded ice. The middle section of the fjord is marked by longer-wavelength negative anomalies (∼−100 nT) and the northern end of the fjord is marked by a long-wavelength high of ∼100 nT on both sides of the fjord (Fig. 5).

In the Petermann fjord, the magnetic basement follows a similar form to the gravity anomaly and corresponding bathymetry (Fig. 5). Reflecting the similarity between the magnetic anomalies on either side of the fjord, the depth to magnetic basement solutions describe a basement surface with the same shape, and at the same depth, on both sides of the fjord. Under the grounded ice, the magnetic basement is coincident with the radar-derived ice bed at ∼500 m depth on the western side, and slightly deeper (∼600 m) on the eastern side. Under the inner basin, depth to basement is up to 500–1000 m lower than the predicted bathymetry but rises in the vicinity of the inner sill, suggesting that a basement structural high influences the sill location. Under the outer basin, where bathymetry has been measured by marine surveys, depth to magnetic basement is ∼2000 m below sea level, indicating a thickness of 700–1300 m of non-magnetic material overlying the basement. No depth solution clusters are identified on either profile between the base of the outer basin and the top of the outer sill. Solutions cluster around the measured depth of the top of the outer sill (∼400 m), suggesting that there is minimal sediment cover over this feature (Fig. 5). Predicted magnetic susceptibility along the profiles shows higher values under the grounded ice and the inner basin (∼0.01 SI), with lower susceptibility over the inner sill (∼0.005 SI) and very low susceptibility over the outer sill (∼0.0005 SI).

4. Discussion

4.1. Geology of Petermann fjord

The bathymetry model presented here includes a linear correction to account for the local variations in density. We now offer further interpretation of the shallow variations in geology along the fjord by combining gravity and magnetic observations with measured bathymetry and mapped geology. Magnetic-basement depth estimates show a similar form to the gravity anomalies, following the ice–rock interface under grounded ice and tracking both the inner and outer sills (Fig. 5). This suggests that both sills have bedrock cores. The close coincidence of magnetic depth and observed bathymetry of the outer sill suggests minimal sediment cover over that sill. The magnetic depth of the inner sill is 300–500 m lower than that predicted by gravity modeling, suggesting some non-magnetic sediment cover. This could be either metasediments similar to those in the fjord walls, or loose sediments deposited within the fjord. To account for the trend in gravity residuals along the fjord, the southern, grounded end of the profile must be underlain by denser material than the northern, seaward end. This requires either that the northern end be made of less dense material – either the Silurian carbonate reefs or a thick pile of loose sediment, or that denser rock exists at the grounding line, such as the crystalline orthogneiss that has been identified in the nearby Victoria fjord (Henriksen et al., 2009; Nutman et al., 2008). It is likely that a combination of these effects contributes to the observed trend.

Guided by the tops of the streaks of clustered magnetic-basement depth solutions in Fig. 5, we show the basement dipping at approximately 1° to the north along the profile, broken by at least one fault. This fault is in line with the Faith Gletscher Fault, exposed on the western wall of Petermann fjord (Fig. 3). With a mapped throw of at least 365 m (Dawes et al., 2000) the Faith Gletscher fault accommodates the change in basement depth between the inner sill and the outer basin and is expressed in the bathymetry as the seaward edge of the inner sill. Although the Faith Gletscher Fault has not been observed in the eastern wall of Petermann fjord, it is shown as present on the eastern profile, where basement depth drops by between 550 m at the northern end of the inner sill.
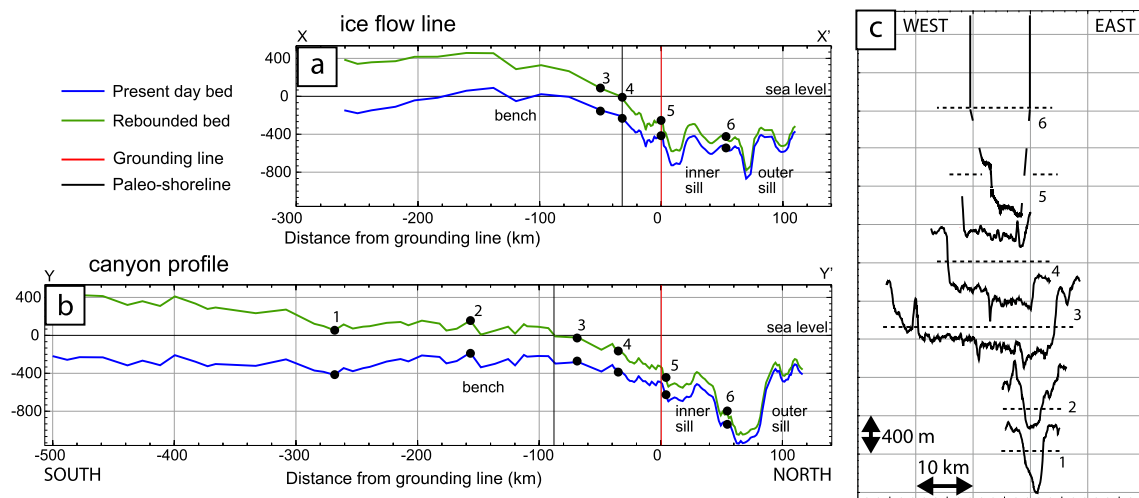
Fig. 6. Longitudinal profile a) across the catchment and b) along the canyon at Petermann Glacier, sampled at points measured by Operation IceBridge MCoRDS radar (locations in Fig. 1). Present day elevation is in blue. Rebounded topography after the removal of the present day ice sheet assuming an elastic thickness of 120 km is in green. c) Cross sectional profiles of the canyon from locations (yellow lines) in Fig. 1a, positions are also marked on profiles here. Dashed line shows present day sea level for each profile. (For interpretation of the references to color in this figure legend, the reader is referred to the web version of this article.)

In these models, basement rock has an assigned density of 3000 kg/m^3, while the metasediments making up the fjord walls are assigned 2670 kg/m^3 and loose sediments 2450 kg/m^3. On the eastern profile, the observed anomaly is well matched (RMS of 2.89 mGal) if the dense basement levels out at ∼2100 m depth under an outer sill with density 2640 kg/m^3. In this scenario, the reef material is slightly less dense than the siliciclastic metasediments of the fjord walls, and is recognized as the low-susceptibility (0.0005 non-dimensional SI units) magnetic basement by the Werner deconvolution solutions. The close match between predicted magnetic basement and observed sill height suggests minimal recent sediment cover on the outer sill.

The western profile has more geological variation than the eastern. The outer basin is 600 m shallower on the west side than the east, as has been confirmed by ship-based surveys. A forward model of this configuration predicts a 41 mGal higher gravity anomaly in the west than the east, but the observed gravity is only 37 mGal higher. Comparison between the eastern and western profiles shows that the observed gravity can be well matched if the excess bed material on the western side is unconsolidated sediment with a density of 2450 kg/m^3.

A second mismatch between predicted and observed gravity occurs over the outer sill. Here, the 2100 m-deep basement and 2640 kg/m^3-density reef material of the eastern side leave a residual of up to 17 mGal on the western side. In order to reduce this residual, we require less mass at the seaward end of the western profile. Magnetic depth to basement estimates closely match the ship-based observed bathymetry, suggesting that the reduced mass is not due to loose sediments on the outer sill. Therefore the outer sill must either have lower density on its western side than its eastern side, or the dense basement is lower on the western side. The latter is our preferred interpretation. A lower density sill requires sediment of 2450 kg/m^3 to give an RMS fit of 3.47 mGal along the profile. It is not clear how such a density variation would occur, other than from a deposit of loose sediments, which is precluded by the magnetic depth to basement. We instead propose that the dense basement under the outer sill has been downthrown by a previously unmapped fault on the southern margin of the outer sill. This fault is downthrown on its northern side, similar to other faults mapped in the region, and the proposed fault is similar to the Faith Gletscher Fault in having stronger expression on the western side of the fjord than the east. This model fits the observed gravity with an RMS of 3.32 mGal.

4.2. Asymmetry of Petermann fjord

The asymmetry observed across Petermann fjord is not typical of the U-shaped fjord morphology observed in most glaciated landscapes (Syvitski and Shaw, 1995). The fjord axis and the submarine escarpment are perpendicular to the strike of geological formations and mapped faults, suggesting that they are not caused by an along-fjord geological boundary.

The deep canyon that can be traced from the middle of Greenland cuts through the onshore part of the Petermann catchment (Fig. 1) on the eastern side (Van der Veen et al., 2007; Bamber et al., 2013b) and is a potential source of asymmetry within the fjord. A longitudinal profile of the canyon, with the present-day ice load removed and the crust rebounded (Fig. 6b), shows that the canyon followed a shallow gradient, just above sea level as it was routed around the hard, igneous body on the eastern side of the bedrock bench in the Petermann catchment. North of 80.3°N 57°W, ∼90 km inland from the grounding line, the profile drops at a steep angle below sea level, suggesting that the entire region where ice flow is confined by a channel has been subject to strong erosion below sea level (Fig. 6). This change in slope of the longitudinal profile marks the dominance of glacial erosion in the fjord. Asymmetry persists in the region between the rebounded coast line and the present day grounding line (Fig. 6c profiles 3 and 4) but is at a minimum at the grounding line where the eastern side is only 70 m deeper than the western side.

Based on the depth to magnetic basement and forward gravity model presented here, the asymmetry within Petermann fjord appears to be caused by an uneven distribution of sediment within the fjord. The strata making up the sides of the Petermann fjord are metasediments, deposited as siliciclastic trough fill. Potential sediment fill for the fjord includes a mixture of the cliff-forming material deposited by slope failure, marine sediments deposited during times of glacial retreat and increased productivity within the fjord, and sediments transported by Petermann Glacier by erosion from its bed. The uneven distribution could result from either preferential deposition on the west side, or preferential erosion on the east. The eastern side of Petermann fjord has more tributary glaciers draining into it (Fig. 3), possibly contributing to stronger glacial erosion of that side. The east side is deeper both within the fjord and at the grounding line, where it appears to have been influenced by the carving of the canyon coming from the interior. This upstream asymmetry may have guided the path of the glacier

in the past, and contributed to preferential erosion on the east, or lateral deposition to the west.

The outer sill is also aligned with the proposed location of the Petermann grounding line at the LGM (England, 1985) and would have provided a stable grounding position. The bedrock-cored inner sill would have presented a similarly stable position that may have punctuated the retreat of Petermann Glacier in the last 20 kyr.

4.3. Influence of bathymetry

Rignot and Steffen (2008) and Münchow et al. (2014) calculated bottom melting rates across the Petermann floating ice tongue. Rignot and Steffen (2008) assumed steady state conditions during detailed 2002 and 2003 surveys of ice velocity and ice thickness fields. In contrast, Münchow et al. (2014) estimated both steady and non-steady contributions to melt for the 2002 to 2012 period using repeat surveys of glacier ice surface and bottom from ATM, ICESat, and ice sounding radar to estimate absolute changes of geoid-referenced glacier ice location. The calculated rates differ between the two studies, which were based on different observation periods and methodologies, but both show a similar pattern of melt rate variation along flow. The region of highest bottom melting from both studies extends from the grounding line to ~25–35 km seaward, where a local melt-rate minimum is observed (Rignot and Steffen, 2008). This minimum coincides with the position of the inner sill that we model with aerogravity data. Melt rate increases again seaward of the inner sill.

Oceanographic studies of Petermann fjord show that there is abundant ocean heat available to support the basal melting of the ice tongue (Johnson et al., 2011) and the variability in melt rate will be influenced by the circulation and mixing of ocean waters within the fjord. The coincidence of a change in calculated bottom melting rate with the position of the newly-identified inner sill suggests bathymetric control on water circulation and mixing. It is known that bottom bathymetry and sills often determine the propagation, flux, and dissipation of kinetic energy that in the ocean influence vertical density stratification and heat flux (Jenkins et al., 2010). A shallow sill would be expected to increase turbulence and mixing and so locally increase the melt rate. The relatively deep inner sill here has the opposite effect, and coincides with a melt rate minimum. The mechanism by which this sill might influence the basal melt rate is not known, suggesting a need for further investigation of the oceanographic processes beneath the Petermann Glacier tongue, incorporating the seafloor bathymetry presented here.

5. Conclusions

A new bathymetry model of the Petermann Glacier fjord, determined from inversion of free-air gravity anomalies, shows a 540–610 m-deep inner sill 25 km seaward of the 410–480 m-deep grounding line. Water thickness over the inner sill is 400 m and allows water access to the grounding line. The inner sill is coincident with the basal-melt minimum calculated along the floating tongue (Rignot and Steffen, 2008). This coincidence suggests that basal melt rates may be influenced by subglacial circulation over the sill. The physics of this interaction are not fully understood, but the bathymetry under the floating tongue should be included in models of ice-ocean interactions at Petermann Glacier and its grounding zone.

The Petermann fjord is up to 600 m deeper on its eastern side than on the west, with a maximum depth of 1150 m. Petermann Glacier has carved 900 m cliffs from the topographic surface down to sea level and a further 1150 m below sea level to the deepest part of the outer basin. The Silurian reef at the head of the

fjord has resisted erosion and provided the northern boundary behind which the glacier over deepened its bed. Onshore mapping of moraines from the LGM give a predicted position of the Petermann Glacier grounding line across this reef (England, 1985), indicating that it provided a stable point for the grounding line in times of greater glaciation.

The close coincidence of the inner sill with faults crossing the fjord suggests that it has a bedrock core. Just as the outer sill likely provided a stable resting position for the grounding line of the Petermann Glacier during the LGM, the inner sill could have provided a stabilizing point for the grounding line during its retreat, causing a dynamically-driven pause in its retreat history.

References

Allen, C., 2011. Icebridge Mcords l2 Ice Thickness. NASA DAAC at the National Snow and Ice Data Center, Boulder, CO, USA.

Argyle, M., Ferguson, S., Sander, L., Sander, S., 2000. AIRGrav results: a comparison of airborne gravity data with GSC test site data. Lead. Edge 19, 1134–1138.

Balmino, G., Vales, N., Bonvalot, S., Briais, A., 2011. Spherical harmonic modeling to ultra-high degree of Bouguer and isostatic anomalies. J. Geod.

Bamber, J., Griggs, J., Hurkmans, R., Dowdeswell, J., Gogineni, S., Howat, I., Mouginot, J., Paden, J., Palmer, S., Rignot, E., Steinhage, D., 2013a. A new bed elevation dataset for Greenland. Cryosphere 7, 499–510.

Bamber, J.L., Siegert, M.J., Griggs, J.A., Marshall, S.J., Spada, G., 2013b. Paleofluvial mega-canyon beneath the central Greenland ice sheet. Science 341 (6149), 997–999.

Bengaard, H.-J., Henriksen, N., 1991. Sedimentary basins of North Greenland. In: Bulletin Grønlands Geologiske Undersøgelse, vol. 160. Loose map Geological map of North Greenland, 1:1000000.

Boghosian, A., Tinto, K., Cochran, J., Porter, D., Eliaff, S., Burton, B., Bell, R., submitted for publication. Resolving fjord bathymetry from airborne gravity along Greenland fjords.

Cochran, J., Bell, R., 2011. IceBridge Sander AIRGrav L1B Geolocated Free Air Gravity Anomalies. National Snow and Ice Data Center.

Cochran, J., Burton, B., Frearson, N., Tinto, K., 2011. IceBridge Scintrex CS-3 Cesium Magnetometer L1B Geolocated Magnetic Anomalies. National Snow and Ice Data Center.

Dawes, P., Frisch, T., Garde, A., Iannelli, T., Ineson, J., Jensen, S., Pirajno, F., Sønderholm, M., Stemmerik, L., Stouge, S., Thomassen, B., van Gool, J., 2000. Kane basin 1999: mapping, stratigraphic studies and economic assessment of Precambrian and lower Paleozoic provinces in north–western Greenland. Geol. Greenl. Surv. Bull. 186, 11–28.

England, J., 1985. The late quaternary history of hall land, northwest Greenland. Can. J. Earth Sci. 22, 1394–1408.

Escher, J. Pulvertaft, T., 1995. Geological Map of Greenland, 1:2500000. Geological Survey of Greenland, Copenhagen.

Henriksen, N., Higgins, A., Kalsbeek, F., Pulvertaft, T., 2009. Greenland from Archaen to Quaternary. Descriptive text to the 1995 Geological map of Greenland, 1:2500000. In: Geological Survey of Denmark and Greenland, 2nd edition. In: Geological Survey of Denmark and Greenland Bulletin, vol. 18.

Jenkins, A., Dutrieux, P., Jacobs, S., McPhail, S., Perrett, J., Webb, A., White, D., 2010. Observations beneath Pine Island Glacier in West Antarctica and implications for its retreat. Nat. Geosci. 3, 468–472.

Jensen, S., 1998. Carbonate-hosted Zn–Pb–Ag mineralisation in Washington land, western north Greenland. Geol. Greenl. Surv. Bull. 180, 67–72.

Jepsen, H., Henriksen, N., Hurst, J., Peel, J., 1983. Geology, 1:250000, Washington Land and Daugaard–Jensen Land. Geological Survey of Greenland, Copenhagen.

Johnson, H., Münchow, A., Falkner, K., Melling, H., 2011. Ocean circulation and properties in Petermann fjord, Greenland. J. Geophys. Res. 116 (C01003), 18.

Khan, S., Wahr, J., Bevis, M., Velicogna, I., Kendrick, E., 2010. Spread of ice mass loss into northwest Greenland observed by grace and GPS. Geophys. Res. Lett. 37 (L06501), 5 pp.

Krabill, W., Abdalati, W., Frederick, E., Manizade, S., Martin, C., Sonntag, J., Swift, R., Thomas, R., Yungel, J., 2002. Aircraft laser altimetry measurement of elevation changes of the Greenland ice sheet: technique and accuracy assessment. J. Geodyn. 34 (3–4), 357–376.

Leuschen, C., 2012. IceBridge MCoRDS L2 Ice Thickness. National Snow and Ice Data Center.

Moon, T., Joughin, I., Smith, B., Howat, I., 2012. 21st-century evolution of Greenland outlet glacier velocities. Science 336 (6081), 576–578.

Münchow, A., Padman, L., Fricker, H., 2014. Interannual changes of the floating ice shelf of Petermann gletscher, north Greenland, from 2000 to 2012. J. Glaciol. 60 (221), 489–499.

Nick, F., Luckman, A., Vieli, A., Van der Veen, C., Van As, D., Van der Wal, R., Pattyn, F., Hubbard, A., Floricoiu, D., 2012. The response of Petermann Glacier, Greenland, to large calving events, and its future stability in the context of atmospheric and oceanic warming. J. Glaciol. 58 (208), 229–239.

Nutman, P., Dawes, P., Kalsbeek, F., Hamilton, M., 2008. Palaeoproterozoic and Achaean gneiss complexes in northern Greenland: Palaeoproterozoic terrane assembly in the high arctic. Precambrian Res. 161 (3–4), 419–451.

Porter, D., Tinto, K., Boghosian, A., Cochran, J., Bell, R., Manizade, S., Sonntag, J., 2014. Bathymetric control of tidewater glacier mass loss in northwest Greenland. Earth Planet. Sci. Lett. 401, 40–46.

Pritchard, H.D., Arthern, R.J., Vaughan, D.G., Edwards, L.A., 2009. Extensive dynamic thinning on the margins of the Greenland and Antarctic ice sheets. Nature 461 (7266), 971–975.

Rignot, E., 1998. Hinge-line migration of Petermann gletscher, north Greenland, detected using satellite–radar interferometry. J. Glaciol. 44 (148), 469–476.

Rignot, E., Steffen, K., 2008. Channelized bottom melting and stability of floating ice shelves. Geophys. Res. Lett. 35 (L02503), 5.

Sander, S., Argyle, M., Elieff, S., Ferguson, S., Lavoie, V., Sander, L., 2004. The AIRGrav airborne gravity system. In: Lane, R. (Ed.), Airborne Gravity 2004 – Australia Society of Exploration Geophysicists Workshop. Geoscience Australia, pp. 49–53.

Studinger, M., Bell, R., Frearson, N., 2008. Comparison of AIRGrav and GT-1A airborne gravimeters for research applications. Geophysics 73, 151–161.

Syvitski, J., Shaw, J., 1995. Sedimentology and geomorphology of fjords. In: Perillo, G. (Ed.), Geomorphology and Sedimentology of Estuaries, vol. 53. Elsevier.

Talwani, M., Worzel, J., Landisman, M., 1959. Rapid gravity calculations for two-dimensional bodies with application to the Mendocino submarine fracture zone. J. Geophys. Res. 64, 49–59.

Van der Veen, C., Leftwich, T., von Frese, R., Csatho, B., Li, J., 2007. Subglacial topography and geothermal heat flux: potential interactions with drainage of the Greenland ice sheet. Geophys. Res. Lett. 34 (L12501), 5 pp.

Werner, S., 1953. Interpretation of Magnetic Anomalies at Sheet-Like Bodies. Sverges Geologiska Undersok Arsbook, vol. 43, 508 pp.